Journal of Nuclear Materials 620 (2026) 156371

Contents lists available at ScienceDirect

Journal of Nuclear Materials

journal homepage: www.elsevier.com/locate/jnucmat

Atomistic insights into the interfacial stability of graphene-reinforced Ni-based alloy composites after cumulative recoil events

Hai Huang [a,*], Xu Yu [a], Yanxin Jiang [a], Qing Peng [c], Guanyu Liu [a], Xiaobin Tang [b,*]

[a] Key Laboratory of Material Physics, Ministry of Education, School of Physics, Zhengzhou University, Zhengzhou 450001, China
[b] Department of Nuclear Science & Technology, Nanjing University of Aeronautics and Astronautics, Nanjing 210016, China
[c] School of Power and Mechanical Engineering, Wuhan University, Wuhan 430072, China

HIGHLIGHTS

- GRMMCs face challenges in maintaining interfacial stability under extreme conditions.
- Solute progressively penetrates Gr, thickening interface and forming metal-carbide bonds.
- Gr exhibits self-healing capabilities, balancing amorphous and crystalline phases.
- Structural survival decays nonlinearly, stabilizing around 17.9 % after 1000 cascades.
- Gr damage evolution follows a four-stage progression impacted by solute interactions.

GRAPHICAL ABSTRACT

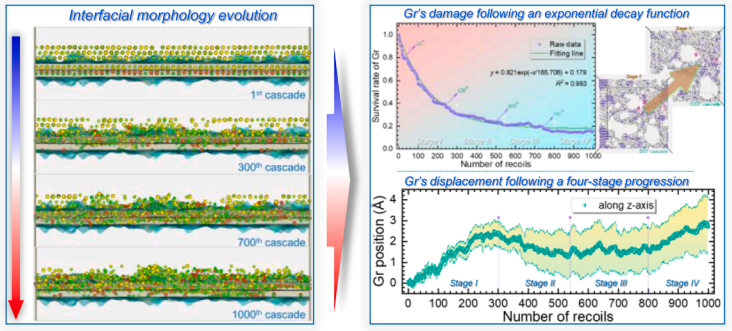

ARTICLE INFO

Keywords:
Graphene/Ni-based alloy interface
Cumulative recoils
Interfacial evolution
Graphene damage
Radiation-induced carbides
Atomistic simulations

ABSTRACT

Graphene (Gr)-reinforced metal matrix composites demonstrate excellent irradiation tolerance but face challenges in maintaining interfacial stability under extreme conditions. Using atomistic simulations, this study examines the evolution of the Gr/Ni-based alloy interface under 1000 cumulative recoils (~0.333 dpa). Early cascade collisions minimally affect interfacial atomic order, but prolonged irradiation induces significant structural changes. Solute atoms progressively penetrate damaged Gr regions, thickening the interface. Gr retains portions of its six-membered ring structure and exhibits self-healing capabilities, balancing amorphous and crystalline phases even after extensive irradiation. Gr's structural survival decays nonlinearly, stabilizing around 17.9 % after 1000 cascades. The damage evolution of Gr follows a four-stage progression characterized by distinct z-axis migration patterns influenced by solute atom interactions. Despite localized damage and disorder, Gr largely resists dissolution, maintaining its stabilizing role in interfacial integrity. Irradiation induces exponential decay of carbon-carbon bonds but growth of M–C bonds (where M denotes solute), paradoxically favoring metal-carbide formation over sp^3 conversion. Furthermore, carbides nucleate preferentially at curled edges of Gr. These findings offer valuable insights into the irradiation-induced evolution of the composites for nuclear applications.

* Corresponding authors.
E-mail addresses: huanghai@zzu.edu.cn (H. Huang), tangxiaobin@nuaa.edu.cn (X. Tang).

https://doi.org/10.1016/j.jnucmat.2025.156371
Received 29 September 2025; Received in revised form 25 November 2025; Accepted 9 December 2025
Available online 9 December 2025

1. Introduction

Derived from Gen-IV nuclear power technology, heat pipe-cooled reactors (HPCRs) possess inherent safety characteristics, including a compact layout, simplified design, intrinsic dependability, and suitability for autonomous operation—making them promising candidates for specialized applications in space propulsion, subsea power units, and decentralized microreactors in isolated regions [1–3]. Nevertheless, the viability of HPCRs hinges critically on the long-term integrity and performance of their constituent structural materials. These materials endure significant irradiation-induced damage from high-energy particles within the reactor core's aggressive environment [4–6]. Substantial microstructural deterioration often results from high-dose neutron exposure, primarily via the creation of point defects such as vacancies and self-interstitial atoms. Such defects subsequently undergo self-organization, giving rise to numerous clusters—notably dislocation loops and voids—that propagate extensively throughout the material [6,7]. Consequently, these irradiation-induced alterations can instigate a cascade of detrimental effects, including hardening, embrittlement, swelling, and blistering, which collectively contribute to the premature degradation of critical components [6–8].

Graphene (Gr)-reinforced metal matrix composites (GRMMCs) have shown significant potential for excellent irradiation tolerance, based on both experimental and simulation data, making them promising candidate structural materials for next-generation nuclear reactors [9–18]. For example, Si et al. [12] observed that a Gr/W nanolayer with a reduced period thickness exhibits exceptional tolerance to irradiation, notably in reducing the density of helium bubbles. Liu et al. [13] found that, in comparison to an unreinforced matrix, the Gr/Al composite demonstrates considerably reduced irradiation-induced hardening, improved elongation, lower lattice expansion, and a distinct deformation mechanism following irradiation. Huang et al. [16,17] illustrated that the Gr/Ni interface is capable of attracting, absorbing, and eliminating interstitials, vacancies, as well as helium atoms or clusters, thereby significantly reducing residual irradiation defects. Yang et al. [18] showed that the Gr/Cu interface offers superior defect annihilation capabilities relative to high-angle grain boundaries in copper. However, challenges remain in advancing GRMMCs as candidate structural materials for the advanced nuclear reactors. Among them, a critical area of unresolved research is the reaction between the matrix elements (e.g., Al, Cr, Fe, Mo, Ti) and the C atoms of damaged Gr under high temperature and irradiation conditions, which may lead to the formation of metal carbides [19–23]. The adsorption of these carbides onto the Gr surface may substantially modify the interfacial configuration, which could consequently affect its efficacy for trapping irradiation-induced defects [13,21,22].

To carefully investigate this matter, selecting an alloy where the solvent element does not dissolve in Gr but where the solute may react with it, as the composite's matrix, could be a more effective strategy [20,21]. This is important because if the solvent element interacts too readily with Gr, it may lead to excessive reactions that could disrupt the intrinsic structure of Gr or even result in its complete dissolution from the outset [24–27]. Fortunately, several studies have demonstrated that metallic nickel exhibits minimal reactivity with Gr, and it is also a commonly used structural material in advanced nuclear reactors [7,21,28–30]. Nonetheless, another significant challenge is that the current experimental techniques fall short of directly capturing these complex transformations in real-time or elucidating the underlying physical principles, as these processes occur across multiple scales, both temporally and spatially, from atomic to macroscopic [4–8]. Given experimental constraints, especially at the nanoscale and atomic scale, classical molecular dynamics (MD) emerges as a highly suitable approach for investigating irradiation effects on the Gr/metal interfaces, since it can offer detailed atomic-level insights into damaged microstructure within picosecond-nanometer dimensions [6–8,13]. Consequently, Ni-based alloys with solutes such as Cr and Fe represent an advantageous composite matrix for responding to the above strategy. Meanwhile, the use of MD simulations may appear extremely convenient for studying their interfacial stability under irradiation conditions and understanding the underlying irradiation resistance mechanisms.

In this work, the GH3535 alloy, composed primarily of Ni with 17 wt. % Mo, 7 wt. % Cr, and 4 wt. % Fe [7,31], was utilized as the matrix for a Gr-reinforced Ni-based alloy composite to examine interfacial evolution induced by 1000 cumulative recoil events using MD simulations. Cumulative recoil events may significantly alter the interfacial structural morphology, involving alloy element migration, carbon diffusion, and reaction kinetics in Gr's damaged regions. Because these processes are complex, this study primarily focuses on how Gr's integrity affects interfacial stability, leaving other topics for future research. The selection of the GH3535 alloy as the composite matrix stems from its widespread application as a structural material in heat pipe-cooled micro molten salt reactors, underscoring its significance in engineering [3,7,31]. Additionally, its solute elements, including Mo, Cr, and Fe, interact with Gr [19–21,28], making it an ideal candidate for investigating the formation and behavior of carbide precipitates at the interfaces under irradiation conditions. Noted that the selection of GH3535 alloy as a representative matrix for investigating irradiation-induced interface stability in Gr-reinforced Ni-based alloy composites also exhibits broader implications. The obtained findings may potentially reflect the general structural properties of Ni-based alloy composites.

2. Simulation methodology

The MD simulations were conducted using the LAMMPS code [32], with visualizations produced through the OVITO software package [33]. A sandwich-structured Gr/GH3535 interface model [34], measuring $107.2 \times 107.9 \times 124.3$ Å^3 and consisting of 133,300 atoms, was constructed. Within the alloy matrix, Cr and Fe atoms were randomly distributed at concentrations of 7.82 at. % and 4.16 at. %, respectively, both of which are identical to those found in the actual GH3535 alloy [7,31]. The interactions among Ni, Cr, and Fe atoms were modeled using the embedded atom method (EAM) potential developed by Bonny et al. [35], while those among C atoms in Gr were described using the adaptive intermolecular reactive empirical bond order (AIREBO) potential [36]. Interactions between Ni–C, Cr–C, and Fe–C atoms were represented using the Lennard–Jones and Tersoff-like bond order potentials, respectively, both augmented with short-range ZBL corrections to accurately capture repulsive interactions [34,37,38]. Notably, Mo atoms, which have the highest solute concentration in the GH3535 alloy, were excluded due to the absence of a suitable potential for Ni–Mo–Cr–Fe interactions, particularly in combination with short-range ZBL interactions [38]. As a result, the GH3535 alloy was simplified to a Ni–Cr–Fe system in this study. This simplification, however, does not undermine the hypothesis being investigated nor compromise the qualitative analysis of interfacial evolution influenced by solute elements.

To alleviate internal stress, the interface model underwent relaxation using conjugate gradient minimization (see Fig. 1(a)) and was subsequently equilibrated at approximately zero pressure at 700 K for 100 ps under periodic boundary conditions. The atomic potential energy distribution in the ground state is shown in Fig. 1(b). During static relaxation, a clear segregation of Cr and Fe atoms towards the interface is observed, leading to the formation of numerous vacancies in the adjacent metal atom layer near the Gr. The potential energy distribution further supports the observation that this segregation is driven by the lower potential energy of Cr and Fe atoms at the interface. Notably, the potential energy of Fe reaches as low as −11.26 eV. In contrast, the minimum potential energy of C atoms on Gr is approximately −11.75 eV, significantly lower than the −7.90 eV observed for C atoms at a pure Gr/Ni interface [34]. These findings suggest that Cr and Fe atoms exhibit a strong tendency to form metal carbides with C atoms at the interface, resulting in additional energy release from the system. In addition, the

alloy matrix shows a slight lattice distortion, which is reflected in the fact that the atomic arrangement of the matrix is not perfectly linear but curved, as shown in the inset of Fig. 1(a).

Subsequently, we performed up to 1000 sequential single displacement cascades within the same simulation cell, following the procedure outlined in Refs [39,40]. Each cascade was simulated by imparting a kinetic energy of 5.0 keV to a randomly chosen primary knock-on atom (PKA), with an arbitrary incidence direction, and allowing the system to anneal for 30 ps. A thermal sink was applied at the boundaries of the cell to cool the system to 700 K following the recoil event. Additionally, each cascade model was relaxed for another 30 ps to quickly release the system stress, during which the system was rapidly quenched to 0.1 K and then re-equilibrated at 700 K. Notably, the selected incident energy of 5.0 keV represents a typical value derived from the full PKA energy spectrum in irradiation experiments conducted at MeV energies. This choice allows the use of a reasonably sized simulation cell while achieving damage levels comparable to experimental conditions.

3. Results

3.1. Interface structure analysis before irradiation

To gain deeper insights into the progression of damage following irradiation, the atomic arrangement of the Gr/GH3535 interface model after 100 ps of thermal relaxation before irradiation, along with the diffusion trajectories of various types of atoms during this interval, were analyzed, as illustrated in Fig. 2. When compared to the onset of thermal relaxation (refer to Fig. 1), the interface model exhibits minimal changes, particularly in the bulk region (see Fig. 2(a)). Furthermore, despite the potential for carbide formation on the Gr surface due to the segregation of Cr and Fe atoms nearby, the Gr's intrinsic structure remains intact after 100 ps, with its two-dimensional planar arrangement preserved (see Fig. 2(b)). However, the C atoms on the Gr surface demonstrate directional migration along the xy-plane during thermal relaxation, as indicated by the arrows in Fig. 2(c). This migration varies in magnitude across the Gr plane, with some regions exhibiting significant movement and others very little. This uneven behavior likely arises from lattice mismatches between the Gr layer and the alloy matrix [34]. The migration of metal atoms predominantly occurs within the interfacial region, and similar to the behavior of Gr, most metal atoms exhibit in-plane motion along the xy-plane (see Figs. 2(d – f)). For example, Cr and Fe atoms exhibit greater mobility along the xy-plane at the interface compared to their behavior in the bulk, suggesting that they remain only loosely bound after entering the interface. Among these, Fe atoms are most restricted to in-plane migration at the interface, with no observable movement along the z-axis. Conversely, certain Ni and Cr atoms exhibit noticeable out-of-plane diffusion. Specifically, Cr atoms predominantly migrate toward the interface, while Ni atoms may either move into the interface or escape into the bulk. Cr atoms show the most substantial out-of-plane migration, crossing multiple atomic layers. The underlying causes of these phenomena can be summarized as follows. Fe atoms, possessing the deepest potential well near the interface (see Fig. 1), quickly settle into the interface at the start of the relaxation process. Cr atoms, with the second deepest potential well (see Fig. 1), also move readily into the interface, but due to their higher concentration relative to Fe, they are not fully incorporated initially and are instead gradually captured during relaxation. The migration of Cr and Fe atoms into the interface creates vacancies in their original regions, which facilitates the movement of Ni atoms toward the interface via vacancy exchange. Additionally, due to the "loading-unloading" effect [41], some Ni atoms already at the interface may also be emitted into the bulk region, where they recombine with or annihilate the vacancies.

3.2. Evolution of atomic mixing near the interface during irradiation

Fig. 3 illustrates the distribution of atoms within a specified range near the interface after various numbers of cascade collisions, with the top-down view provided in Fig. S1. Note that the observation region was arbitrarily chosen, with a fixed coordinate range applied for comparison. To examine the diffusion of solute atoms and potential metal-carbide formation, the visualization of Ni atoms was omitted. The interfacial region and the initial z-position of Gr before irradiation are referenced in each panel of Fig. 3, allowing for analysis of the irradiation's impact on the interface structure. After the first cascade, the interface structure remains largely unchanged. By the 50th cascade, the interface maintains its atomic ordering well, and the solute atoms near the interface are minimally affected, despite considerable damage to the Gr. A

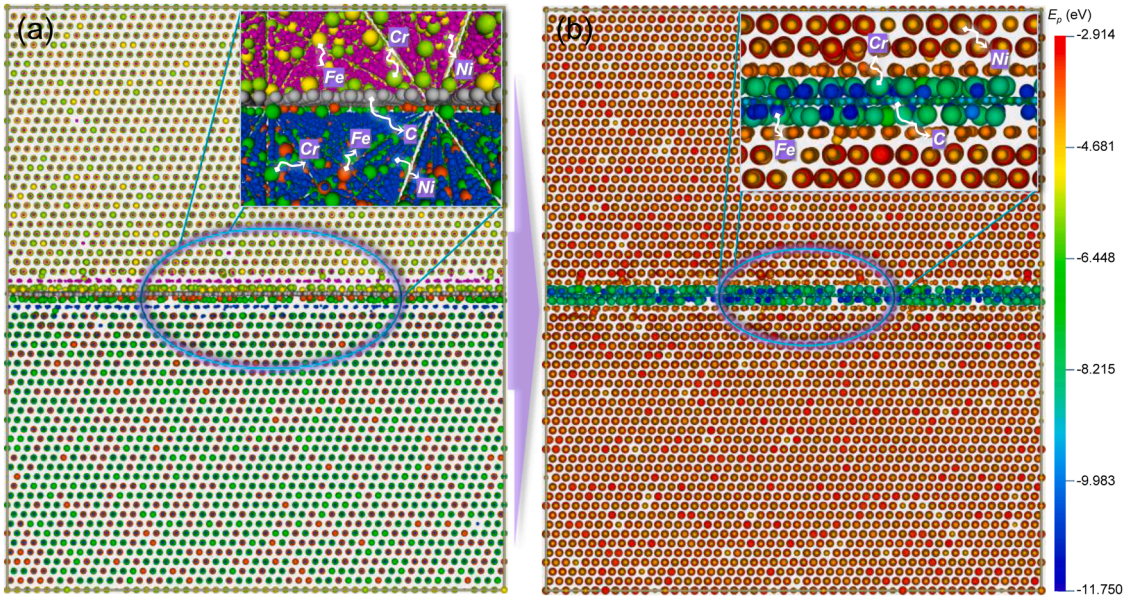

Fig. 1. Model of the Gr/GH3535 interface in the ground state. (**a**) Atomic configuration of the model. (**b**) Model potential energy distributions colored by atomic potential energy, in which the identification of atomic types is based on their respective sizes, with Cr being the largest, followed by Fe, Ni, and C atoms in decreasing order. Atomic types in both subfigures are identified in their respective insets.

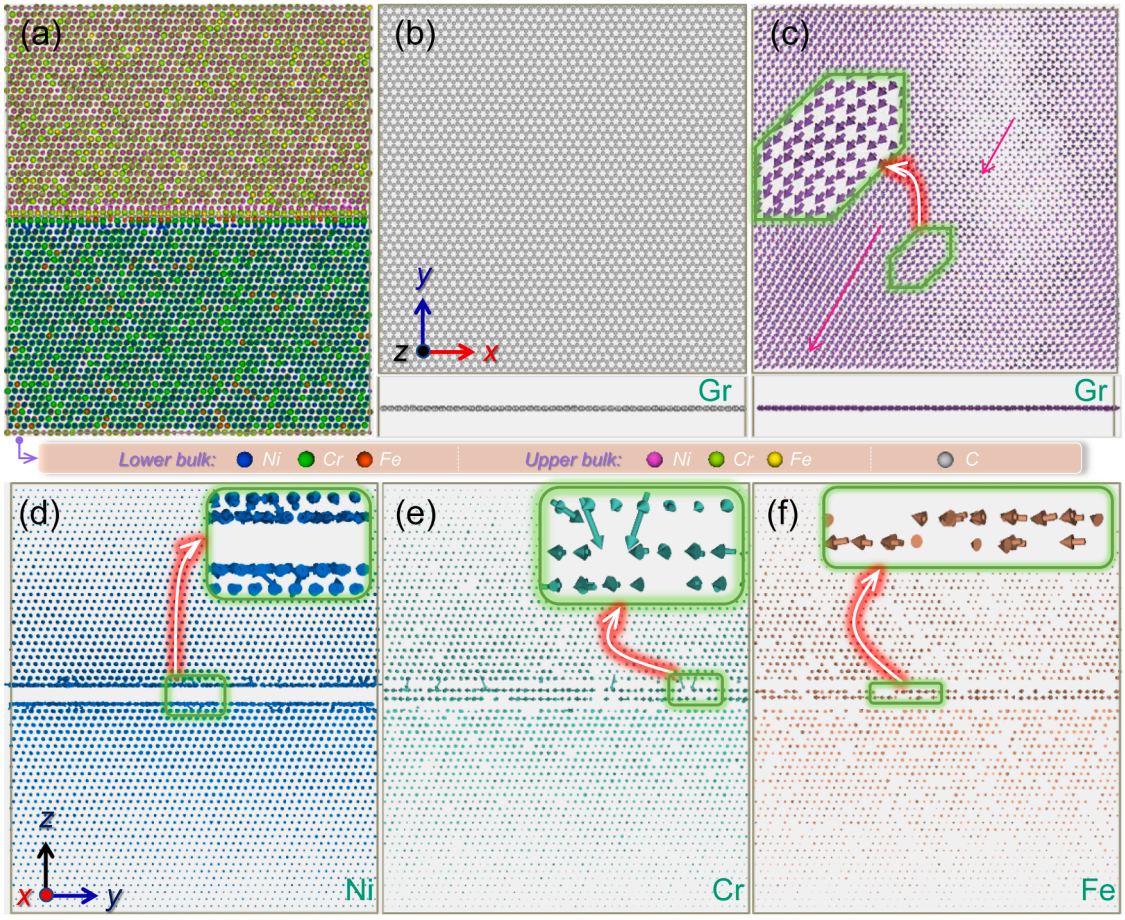

Fig. 2. Evolution of the Gr/GH3535 interface model during thermal relaxation at 100 ps. (**a**) Snapshot of the atomic model following 100 ps of thermal relaxation. (**b**) Snapshoot of the Gr extracted from the panel (a), showing the spatial distribution of C atoms. (**c**−**f**) Displacement trajectories of C (c), Ni (d), Cr (e), and Fe (f) atoms during this period, in which the arrows represent atomic displacement vectors and the insets exhibit the zoomed-in regions of significant atomic displacement.

comparison between the first and 50th cascades reveals that these initial cascades have a limited effect on the interface structure, while Fe atoms at the interface become more strongly bonded to the Gr. Following the 100th cascade, the Gr experiences further damage, enabling solute atoms to break through the Gr barrier and penetrate into the opposite side; for example, Fe atoms from the lower matrix appear in the upper matrix. Simultaneously, more solute atoms enter the interface, causing it to appear more swollen. After the 200th cascade, a more pronounced effect is observed as the Gr begins to deviate significantly from its initial z-position and moves upward. At this point, the solute atoms at the interface predominantly surround the C atoms of Gr, with fewer solute atoms found in the hole regions of the Gr layer. By the 300th cascade, this trend becomes more apparent, with solute atoms concentrating around the C atoms at the damaged edges of Gr. A significant portion of the solute atoms near the interface has been captured by it, with few remaining in the observed bulk region. After the 400th cascade, compared to the 300th cascade, Cr and Fe atoms distant from the interface have largely entered the interface, suggesting the interface's enhanced capacity to capture solute atoms. By the 500th cascade, an increasing number of Cr and Fe atoms are adsorbed by the C atoms on the Gr surface, significantly thickening the interface structure. After the 600th cascade, the primary damage area in Gr stabilizes, and further changes are minimal, with new damage occurring mainly in the original Gr structure. Some localized regions at the interface become thicker, likely due to the ongoing adsorption of Cr and Fe atoms onto the curling C atoms at the damaged edges of Gr. In some small damaged areas of Gr, a healing phenomenon is observed. After the 1000th cascade, the solute atoms around the interface, as observed, essentially disappear, having been absorbed into the interface, resulting in a more complex interfacial structure. At this stage, the Gr's overall structure has migrated to the outermost position of the initial interface along the z-axis.

4. Discussion

4.1. Evolution of graphene morphology during irradiation

The preceding findings demonstrate that cumulative recoil events significantly compromise the integrity of Gr, thereby altering the interfacial structural morphology. Generally, Gr's integrity is prioritized as it is a key part of the interface, and changes to its structure could directly influence how well the interface captures irradiated defects [15,16,18]. To elucidate the damage pattern of Gr during overlapping cascades, we examined the evolution of its intrinsic structure—specifically, the sp^2-hybridized C atoms—using the Polyhedral Template Matching (PTM) toolkit in OVITO [42]. The preservation of Gr's intrinsic structure was quantified by calculating the survival rate, defined as the ratio of the number of sp^2-hybridized C atoms that maintain Gr-like characteristics after each recoil event ($n_{C\_perfect}$) to the total number of sp^2-hybridized C atoms in pristine Gr (n_{C_total}), as depicted in Fig. 4(a). This survival rate declines with an increasing number of cascades, approximating an exponential decay function: $y = 0.821\exp(-x/165.706) + 0.179$, with the decay constant λ defined as 1/165.706 (approximately 0.006). When scaled to temporal dimensions using the 60 ps cascade-annealing cycle duration, the decay constant becomes the decay constant becomes $1/(60 \times 165.706)$ ps^{-1}. The mean lifetime τ of Gr's intrinsic structure, obtained by inverting this temporal decay constant, is calculated as $\tau = 60$

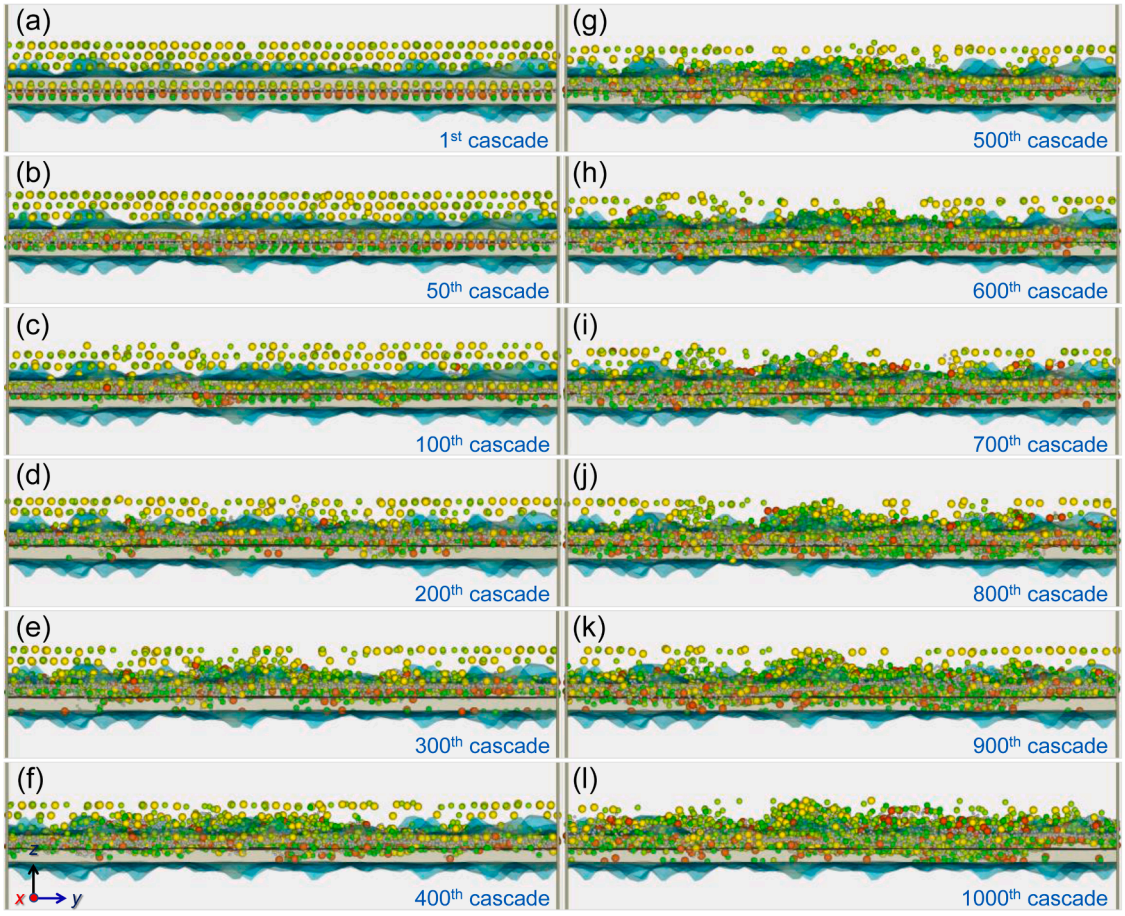

Fig. 3. Cross-sectional snapshots of the distribution of atoms within a specified range near the interface after various numbers of cascades, in which the black line and semi-transparent mesh surface at the center of each panel denote the initial positions of the Gr and the interface before irradiation.

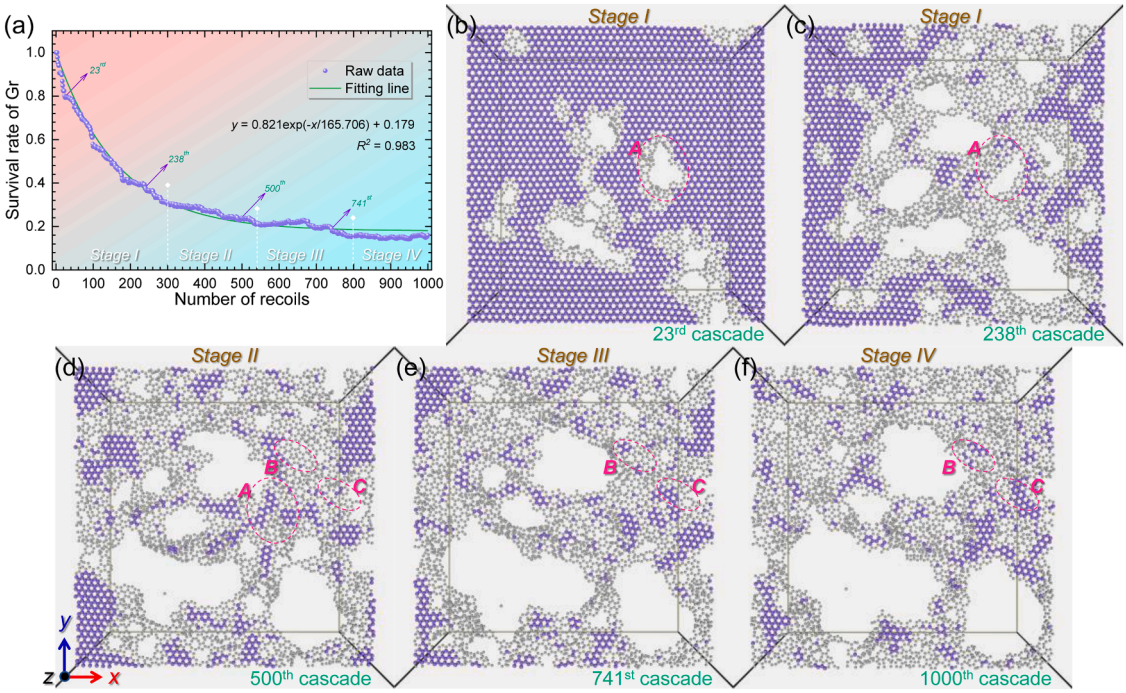

Fig. 4. Evolution of the Gr's intrinsic structure within the interface model after cumulative recoils. (**a**) Survival rate of Gr's intrinsic structure versus the number of cascades. (**b** – **f**) Top-down snapshots of the Gr after the 23 (b), 238 (c), 500 (d), 741 (e), and 1000 (f) cascades, in which the purple and grey spheres represent the Gr-like and amorphous C atoms, respectively.

$\times$ 165.706 $\approx$ 9.942 $\times$ 10^3 ps. Physically, this parameter corresponds to the average duration that *An* sp^2-hybridized C atom maintains its original configuration before transitioning to alternative states—such *A.* sp^3 hybridization or M–C bonding (where M denotes Cr or Fe)—during continuous irradiation. Thus, τ serves as a quantitative indicator for evaluating Gr's structural stability within the irradiated composite system. Typically, simulated irradiation dose rates (on the order of 10^6 dpa·s^{-1}) are orders of magnitude higher than actual rates (usually on the order of 10^{-3} dpa·s^{-1}) [43], leading to an accelerated rate of irradiation damage to the material. Thus, the real mean lifetime is expected to be much longer. Despite the significant discrepancy in dose rates between MD simulations and experiments, recent studies employing similar simulation methods have demonstrated a strong correlation with experimental results [44]. Notably, the survival rate of the Gr's intrinsic structure levels off at approximately 20 % after 800 cascades and slowly approaches the desired value of 17.9 % over time. This observation suggests two key insights: first, prolonged irradiation does not entirely convert Gr into amorphous carbon (or carbide), as it retains portions of its six-membered ring structure, which contrasts with some prior theoretical and experimental predictions [45–47]. Second, Gr may possess a self-healing capability within the composite under nuclear reactor conditions, enabling it to maintain a coexistence of Gr-like and amorphous carbon (or carbide) structures on its surface [16,48–50]. In the current simulations, a 5 keV cascade corresponds to a dose of 3.334 $\times$ 10^{-4} dpa, as determined using the Norgett−Robinson−Torrens (NRT) analytical model ($0.8E_{PKA}/2NE_d$) [39], where N is the total number of atoms in the simulation cell and E_d denotes the threshold displacement energy (approximately 45.0 eV [39]). Consequently, an irradiation dose of 1000 cascades equates to roughly 0.333 dpa, indicating that beyond this irradiation level, Gr sustains a coexistence of Gr-like and amorphous carbon (or carbide) structures, as supported by the aforementioned observations. In our previous experiments on a pure Gr/Ni composite exposed to 300 keV He^{2+} ion [17], the extent of Gr damage at an irradiation dose of 2.4 dpa was estimated using the amorphization trajectory of carbon materials proposed by Ferrari et al. [45], which closely matches the present simulation results. These findings corroborate the accuracy of our simulations and refine theoretical predictions regarding the evolution of Gr damage in the composite at high irradiation doses.

To examine the damage behavior of Gr in detail, four distinct phases were identified based on variations in the decay rate of its structural survival, as indicated in Fig. 4(a): Stage I (0–300 cascades), Stage II (300–540 cascades), Stage III (540–800 cascades), and Stage IV (800–1000 cascades). Note that the boundaries between neighboring phases are approximate, but can effectively capture key trends in structural degradation. Representative damaged Gr structures were selected and analyzed from each stage, with their top-view images shown in Figs. 4(b–F) (see Supplementary Movie 1 for details). After the 23rd cascade (Stage I), the Gr's intrinsic structure is significantly damaged, reducing its structural integrity by 20 %. By the 238th cascade (Stage II), the Gr damage has increased further, reaching 60 %, with the decay rate remaining rapid up to this point. While most damaged regions show a continuous expansion of hole areas, some exhibit anomalous behavior, such as a reduction in damage. For example, in region ***A***, marked in Figs. 4(b) and (c), the hole area decreases significantly after more than 200 cascades. This phenomenon becomes even more pronounced after the 500th cascade (Stage II), where the holes in region ***A*** nearly disappear, and parts of the Gr-like structure are restored (see Fig. 4(d)). This indicates that Gr does not undergo complete decomposition under irradiation, which would otherwise result in the disappearance of the interface; instead, it appears to play a stabilizing role in maintaining the interfacial structure under such conditions. A comparison of the 741st and 1000th cascades reveals that the damage profile of larger holes remains mostly unchanged, undergoing only minor adjustments. Throughout the process, regions of local amorphous carbon (or carbide) on the Gr surface display a notable tendency to revert to the intrinsic six-membered ring (or Gr-like) structure. For example, in regions ***B*** and ***C***, shown in Figs. 4(d–F), the proportion of sp^2-hybridized C atoms that maintain Gr-like characteristics consistently increases, further supporting Gr's self-healing capability. In addition, the development of holes on the Gr, coupled with the diminished Gr-like regions and the rise in amorphous carbon (or carbide), could offer a foundational insight into the irradiation-induced grain refinement of Gr observed in previous experiments on a Gr/Ni composite [17]. Building on this, the findings further reinforce the hypothesis from previous experimental studies that Gr effectively preserves interfacial stability under prolonged irradiation [14,17].

4.2. Displacement behavior of graphene during irradiation

Another notable observation in Fig. 3 is the gradual displacement of Gr from its initial position, migrating upward along the z-axis during cumulative recoil events. To investigate this behavior, the relationship between the z-axis position of Gr and the number of cascades was analyzed, as depicted in Fig. 5(a). During the first 300 cascades, the migration distance along the z-axis increases approximately linearly, reaching its first local maximum at the 300th cascade. Between the 300th and 540th cascades, the migration exhibits a reverse and progressively diminishing pattern. From the 540th to the 700th cascades, the migration fluctuates but remains stable, and after the 700th cascade, it begins to linearly increase again. Notably, the four stages of migration closely align with the stages observed in the Gr' survival rate, leading to the adoption of the same stage classification in subsequent analyses. This migration is likely driven by the interactions of Gr with solute atoms, resulting in a drag force on the Gr [51–54]. The variation in migration direction and the extent of migration are likely linked to the displacement of C atoms on the Gr surface, with details on these observations to be elaborated upon later. The underlying causes of the changes in Gr's z-axis coordinates can be explained as follows. During the first 300 cascades, an increasing number of dangling C atoms emerge on the Gr's upper surface, combining with solute atoms in the upper bulk and experiencing an upward drag force. Between the 300th and 540th cascades, dangling C atoms gradually accumulate on the Gr's lower surface, interacting with solute atoms in the lower bulk and resulting in a downward drag force. From the 540th to the 700th cascades, the drag forces acting on the Gr's upper and lower surfaces become nearly balanced, resulting in minimal net migration. This process repeats cyclically thereafter. The rate of Gr damage directly impacts the number of dangling C atoms and their displacement, which in turn affects the interactions of Gr with solute atoms and ultimately shapes its migration behavior. After 1000 cascades, the total migration distance of Gr is approximately 2.7 Å. However, this is minimal compared to the migration of grain boundaries [40], indicating that the Gr/GH3535 interface remains effectively pinned and highly resistant to movement once formed. Throughout irradiation, the interface essentially stays near its initial position, with only alternating structural changes between Gr-like and amorphous (or carbide) states. Furthermore, the migration mechanism of the Gr/GH3535 interface differs significantly from that of grain boundaries [40].

To further investigate the migration behavior, 1–3 representative damaged Gr structures were selected from each of the four stages for detailed analysis, with their side views depicted in Figs. 5(b − *h*) (see Supplementary Movie 2 for details). After the 100th cascade (Stage I), the intact region of Gr remains largely flat. By the 300th cascade, however, the Gr structure becomes increasingly disordered, with a noticeable increase in thickness, particularly on its upper side. This could create active sites that facilitate enhanced bonding with solute atoms in the upper bulk [24], thereby gradually pulling the Gr upward. Additionally, several sp^2-hybridized C atoms that maintain Gr-like characteristics are observed in areas exhibiting significant out-of-plane disorder in the Gr. At this point, several C atoms, such as those labeled in the regions ***L, M***, and ***N*** in Fig. 5(c), detach from the Gr and migrate into the surrounding matrix. After the 400th cascade (Stage II), some of the

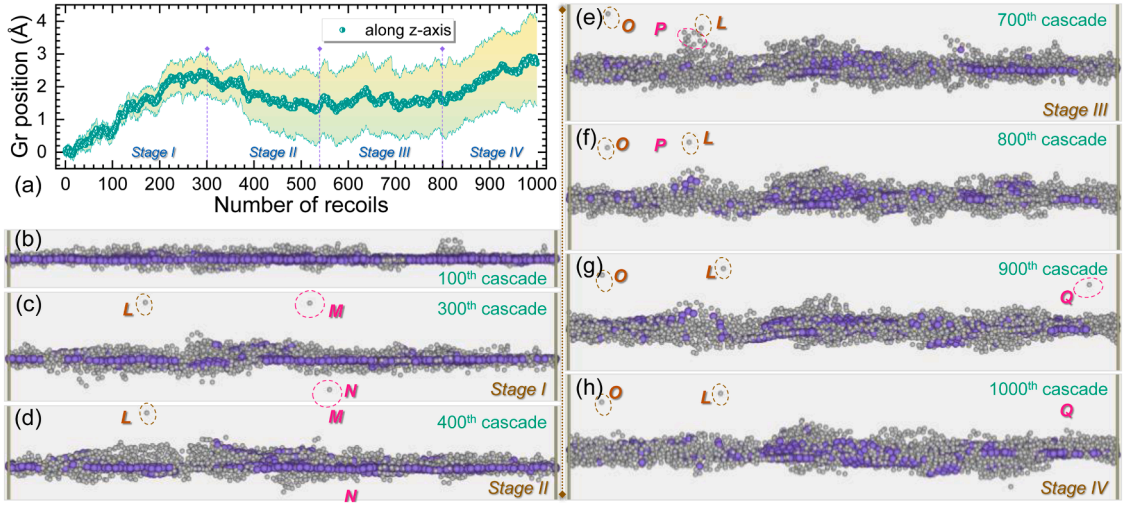

Fig. 5. Displacement of the Gr within the interface model after cumulative recoils. (**a**) z-axis position of Gr as a function of the number of cascades. (**b** — **h**) Cross-sectional snapshots of the Gr after 100 (b), 300 (c), 400 (d), 700 (e), 800 (f), 900 (g), and 1000 (h) cascades, in which the purple and grey spheres represent the Gr-like and amorphous C atoms, respectively.

detached C atoms are reabsorbed by the Gr, as indicated by regions ***M*** and ***N*** in Fig. 5(d). Simultaneously, more and more C atoms accumulate on the lower side of the Gr, providing active sites for solute atoms in the lower bulk. The resulting binding forces drive the Gr to migrate downward. By the 700th cascade, dangling C clusters are observed on the Gr surface, penetrating deeper into the bulk, such as those identified in the region ***P*** of Fig. 5(e). These clusters, however, are often reintegrated into the Gr structure over time (see Fig. 5(f)). After the 800th cascade, the Gr's overall structure, including its level of disorder and thickness, exhibits minimal further changes. However, small dangling C clusters continue to appear on the upper surface, potentially generating a drag force that drives further upward migration. Comparing these observations with Fig. 3 reveals that the Gr structure closely aligns with the interface's overall morphology. This suggests that the sites of the disordered C atom on the Gr serve as nucleation points for solute atoms, thereby significantly influencing their spatial distribution. Throughout the irradiation process, not all C atoms that detach from the Gr and enter the bulk are reabsorbed by the Gr. Conversely, some react with solute atoms in the bulk, forming stable carbides that become permanently retained, as exemplified by the regions ***L*** and ***O*** in Fig. 5(c — *h*). In addition, while prolonged irradiation causes some damage and disorder to the Gr, its C atoms largely remain confined within their bonded framework and resist dispersal into the matrix. This stability prevents the Gr from gradually dissolving, enabling the coexistence of its Gr-like structure with amorphous carbon or carbide phases over extended durations.

4.3. *Formation and evolution of metal carbides during irradiation*

The aforementioned findings emphasize two key irradiation-dependent effects: as the irradiation dose increases, (I) the Gr at the interface sustains progressive damage, generating an increasing number of dangling C atoms, while (II) solute Cr and Fe atoms are continuously trapped and retained at the interface due to interfacial sink effects [16, 18]. Consequently, these trapped solute atoms further combine with the dangling C atoms on the Gr surface, forming M–C bonds, which

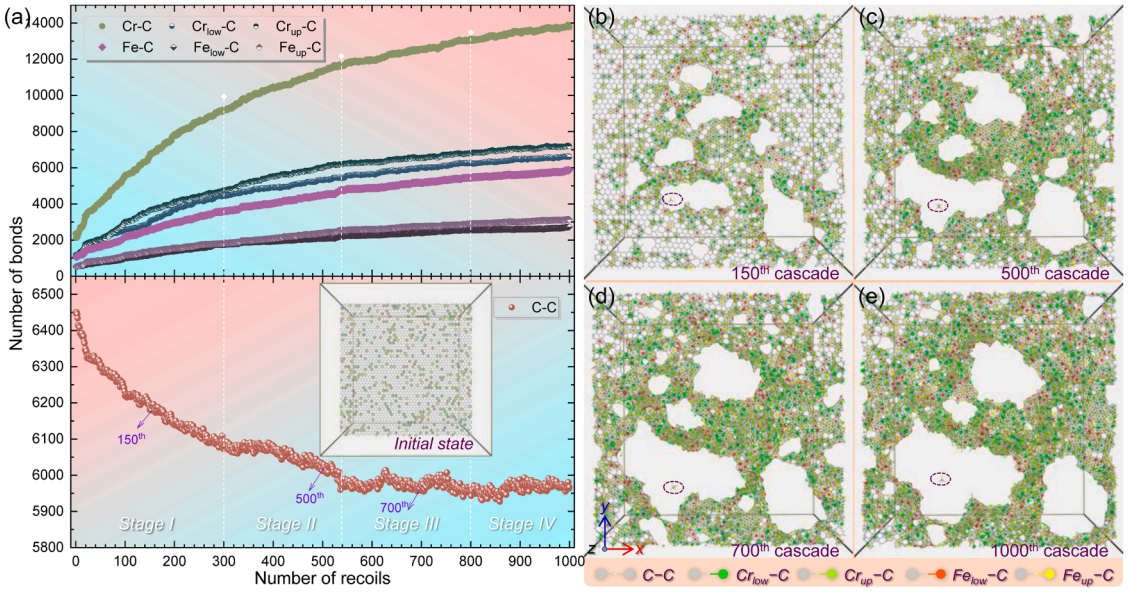

Fig. 6. Evolution of the chemical bonds within the interface model after cumulative recoils. (**a**) Carbon-carbon and M–C bond counts versus cascade number. (**b** — **e**) Top-down snapshots of interfacial bonding configurations after 150 (b), 500 (c), 700 (d), and 1000 (e) cascades, with bond types distinguished by color coding.

subsequently serve as nucleation sites for metal carbides at the interface. To clarify this process, Fig. 6(a) specifically tracks how the counts of carbon-carbon bonds (encompassing C–C, C=C, and C≡C bonds) and M–C bonds evolve with successive cascade collisions. Bond identification was performed using pair-wise distance cutoffs: 1.65 Å for carbon-carbon bonds, 3.1 Å for Cr–C bonds, and 2.7 Å for Fe–C bonds, each marginally exceeding the maximum theoretical bond length [36,37]. Consistent with the intrinsic Gr structural evolution in Fig. 4, the quantity of carbon-carbon bonds displays pronounced exponential decay, plateauing near the 800th cascade with an approximate 7.9 % reduction. In contrast, Cr–C and Fe–C bond counts exhibit exponential growth. Typically, damage to Gr's intrinsic structure promotes a transition from high-energy-barrier sp^2-hybridized C atoms to low-energy-barrier sp^3-hybridized states [17,45], which should theoretically increase carbon-carbon bonds. However, the observed decrease in carbon-carbon bonds alongside the increase in M–C bonds suggests that broken intrinsic C=C bonds preferentially form bonds with Cr or Fe rather than simply converting to sp^3-hybridized carbon. The non-zero initial count of M–C bonds confirms the hypothesis from Figs. 1 and 2, that Cr or Fe atoms trapped at the interface after relaxation form carbides with the C atoms of Gr. Given the preservation of Gr's initial hexagonal lattice integrity, carbide formation at this stage likely originated from cleavage of intrinsic C=C bonds. This process, however, induced no substantial lattice distortion in the Gr structure. Furthermore, Cr–C bonds consistently outnumber Fe–C bonds, attributed to the higher Cr content in the alloy matrix, leading to more Cr atoms reaching the interface to bond with dangling C atoms. Additionally, solute atoms originating above the Gr bond more readily with unsaturated C atoms than those below throughout irradiation, indicative of a stronger upper drag force that further accounts for the predominant upward migration of Gr observed in Fig. 5.

To maintain consistency with the analyses presented in Figs. 4 and 5, the investigation into the formation and evolution of metal carbides was conducted using the same four-stage progression framework (see Fig. 6 (a)). The interfacial bonding configurations typical of each stage were systematically characterized, with corresponding top-view images shown in Figs. 6(b – e) (see Supplementary Movie 3 for details). Following 150 cascade collisions (Stage I), the bonding between solute atoms and carbon demonstrated only a minimal increase in undamaged regions of Gr compared to the pre-irradiation state, but exhibited a marked rise within damaged regions, reinforcing the notion that broken C=C bonds preferentially bind to Cr or Fe atoms. Simultaneously, C atoms displaced into the bulk through cascade collisions formed bonds with neighboring Cr or Fe atoms, as indicated by the dashed ellipses in Fig. 6(b). Upon reaching Stage II (e.g., the 500th cascade), a notable intensification of M−C bonding occurred along the curled edges of Gr, attributed to the increased presence of dangling C atoms, thereby identifying these locations as the principal sites for carbide nucleation. It is noteworthy that regions preserving carbon ring structures, irrespective of their hexagonal nature, consistently exhibited resistance to bonding with solute atoms. These dual patterns persisted throughout the irradiation process, despite significant alterations in the spatial arrangement of M−C bond locations, as illustrated in Figs. 6(d) and (e). Meanwhile, C atoms situated within the bulk became effectively immobilized after bonding with nearby Cr or Fe atoms.

5. Conclusions

In summary, this study has investigated the interfacial evolution in a Gr-reinforced Ni-based alloy composite subjected to cumulative recoil events through MD simulations, with GH3535 alloy serving as a representative matrix system for such composites. The results demonstrate that the Gr/Ni-based alloy interface efficiently captures solute atoms, such as Cr and Fe, during extended irradiation. This process leads to a notable enrichment of solutes at the interface while depleting them from the surrounding bulk regions. The interfacial structure becomes increasingly complex, emphasizing the enhanced adsorption capacity of the interface. Simultaneously, the response of Gr to irradiation reveals a dual-phase coexistence, characterized by partially preserved Gr-like structures alongside regions of amorphous carbon or carbide. Despite substantial irradiation damage, Gr retains approximately 17.9 % of its original structure after 1000 cascades, avoiding complete amorphization or carbide precipitates. Localized self-healing effects further underline Gr's resilience and its critical role in preserving interfacial stability during irradiation. The Gr exhibits minimal migration along the z-axis, with a total displacement of around 2.7 Å after 1000 cascades, reflecting its strong anchoring to the interface. This limited movement, driven by asymmetric interactions with dangling C atoms and solutes, contrasts sharply with the behavior of migrating grain boundaries. While some C atoms detach and are subsequently reintegrated, Gr resists extensive degradation and remains structurally stable. Furthermore, carbon-carbon bonds decay exponentially, while M–C bonds grow exponentially. This paradox, occurring despite expected sp^2-to-sp^3 conversion, confirms preferential bonding of broken C=C bonds with Cr or Fe atoms over sp^3 hybridization. Cr–C bonds dominate due to higher matrix Cr content. Carbides nucleate primarily at the curled edges of Gr, while asymmetric solute bonding above the Gr drives its upward migration. These findings demonstrate Gr's potential to enhance interfacial stability and durability, emphasizing its value as a reinforcement material for composites engineered for high-irradiation environments. Furthermore, this exploratory modeling study provides a generalized insight into irradiation-induced interface stability in GRMMCs, while establishing foundational guidance for forthcoming irradiation experiments on such Ni-based alloy composite systems. This investigation also contributes valuable perspectives for refining theoretical models and supports the application of Gr in advanced alloy systems under extreme operating conditions.

CRediT authorship contribution statement

Hai Huang: Writing – review & editing, Writing – original draft, Visualization, Supervision, Software, Resources, Project administration, Methodology, Investigation, Funding acquisition, Conceptualization. **Xu Yu:** Visualization, Validation, Formal analysis, Data curation. **Yanxin Jiang:** Investigation, Formal analysis, Data curation. **Qing Peng:** Validation, Formal analysis, Data curation. **Guanyu Liu:** Visualization, Formal analysis, Data curation. **Xiaobin Tang:** Writing – review & editing, Supervision.

Declaration of competing interest

The authors declare that they have no known competing financial interests or personal relationships that could have appeared to influence the work reported in this paper.

Acknowledgements

This work was supported by the National Natural Science Foundation of China (Grant No. 12105249), the Young Talent Support Program of Henan Association for Science and Technology (Grant No. 2025HYTP047), the Natural Science Foundation of Henan (Grant No. 252300423007), the Key Project for Science and Technology Development of Henan Province (Grant No. 242102230052), the Training Program for Young Backbone Teachers in Zhengzhou University (Grant No. 2025ZDGGJS010), the Henan Province Postdoctoral Science Foundation (Grant No. 202102012), and the National Supercomputing Center in Zhengzhou.

Supplementary materials

Supplementary material associated with this article can be found, in the online version, at doi:10.1016/j.jnucmat.2025.156371.

Data availability

Data will be made available on request.

References

[1] B. Yan, C. Wang, L. Li, The technology of micro heat pipe cooled reactor: a review, Ann. Nucl. Energy 135 (2020) 106948, https://doi.org/10.1016/j.anucene.2019.106948.

[2] B. Wang, S. Xu, B. Wang, W. Wang, Y. Liu, T. Li, S. Hu, J. Zhang, M. Wang, Review of recent research on heat pipe cooled reactor, Nucl. Eng. Des. 415 (2023) 112679, https://doi.org/10.1016/j.nucengdes.2023.112679.

[3] D. Cui, Y. Dai, X. Cai, F. Fu, X. Li, Y. Zou, J. Chen, Preconceptual nuclear design of a 50 kWth heat pipe cooled micro molten salt reactor (micro-MSR), Prog. Nucl. Energ. 134 (2021) 103670, https://doi.org/10.1016/j.pnucene.2021.103670.

[4] L. Ma, T. Liu, B. Cai, Z. Liu, G. Zhang, J. Li, H. Li, H. Huang, Molecular dynamics studies of primary irradiation damage in α-type Ti35 alloy, Phys. Status Solidi B 260 (2023) 2200560, https://doi.org/10.1002/pssb.202200560.

[5] C.S. Becquart, C. Domain, Modeling microstructure and irradiation effects, Metall. Mater. Trans. A 42 (2011) 852–870, https://doi.org/10.1007/s11661-010-0460-7.

[6] K. Nordlund, S.J. Zinkle, A.E. Sand, F. Granberg, R.S. Averback, R.E. Stoller, T. Suzudo, L. Malerba, F. Banhart, W.J. Weber, F. Willaime, S.L. Dudarev, D. Simeone, Primary radiation damage: a review of current understanding and models, J. Nucl. Mater. 512 (2018) 450–479, https://doi.org/10.1016/j.jnucmat.2018.10.027.

[7] Z. Zhu, R. Qiu, L. Chang, G. Ma, H. Deng, H. Huang, The effect of stress state and He concentration on the dislocation loop evolution in Ni superalloy irradiated by Ni^{+} & He^{+} dual-beam ions: in-situ TEM observation and MD simulations, J. Mater. Sci. Technol. 212 (2025) 77–88, https://doi.org/10.1016/j.jmst.2024.06.015.

[8] Y. Ye, L. Ma, T. Tang, T. Liu, F. Chen, X. Ge, Y. Jiang, X. Yu, H. Huang, Characterization of microstructure and properties of Ti35 alloy and its high-fluence hydrogen irradiation-induced surface exfoliation, Eur. Phys. J. Plus 139 (2024) 822, https://doi.org/10.1140/epjp/s13360-024-05614-0.

[9] Q. Yan, Z. Zhang, H. Guo, Y. Wang, Physical properties and effect of helium-vacancy pair on tungsten/graphene composite as plasma-facing materials from first principles, Fusion Sci. Technol. 80 (2024) 178–195, https://doi.org/10.1080/15361055.2023.2213811.

[10] T. Liu, X. Yuan, H. Huang, Primary irradiation damage in Ni–graphene nanocomposites with pre-existing hydrogen: insights from atomistic simulations, Eur. Phys. J. Plus 139 (2024) 22, https://doi.org/10.1140/epjp/s13360-023-04812-6.

[11] Y. Liu, J. Zhang, L. Zhao, Q. Guo, Helium-bubble-assisted deformation twinning in irradiated graphene (reduced graphene oxide)-aluminum composite with a nanolaminated structure, J. Nucl. Mater. 545 (2021) 152741, https://doi.org/10.1016/j.jnucmat.2020.152741.

[12] S. Si, W. Li, X. Zhao, M. Han, Y. Yue, W. Wu, S. Guo, X. Zhang, Z. Dai, X. Wang, X. Xiao, C. Jiang, Significant radiation tolerance and moderate reduction in thermal transport of a tungsten nanofilm by inserting monolayer graphene, Adv. Mater. 29 (2017) 1604623, https://doi.org/10.1002/adma.201604623.

[13] Y. Liu, Y. Zeng, Q. Guo, J. Zhang, Z. Li, D. Xiong, X. Li, D. Zhang, Bulk nanolaminated graphene (reduced graphene oxide)–aluminum composite tolerant of radiation damage, Acta Mater. 196 (2020) 17–29, https://doi.org/10.1016/j.actamat.2020.06.018.

[14] L. He, S. Si, H. Xu, C. Tang, J. Liu, S. Dong, C. Jiang, X. Xiao, Enhanced mechanical property and radiation resistance of reduced graphene oxide/tungsten composite with nacre-like architecture, Compos. Struct. 245 (2020) 112361, https://doi.org/10.1016/j.compstruct.2020.112361.

[15] T. Yang, L. Yang, H. Liu, H. Zhou, S. Peng, X. Zhou, F. Gao, X. Zu, Ab initio study of stability and migration of point defects in copper-graphene layered composite, J. Alloy. Compd. 692 (2017) 49–58, https://doi.org/10.1016/j.jallcom.2016.08.311.

[16] H. Huang, X. Tang, K. Xie, Q. Peng, Enhanced self-healing of irradiation defects near a Ni–graphene interface by damaged graphene: insights from atomistic modeling, J. Phys. Chem. Solids 151 (2021) 109909, https://doi.org/10.1016/j.jpcs.2020.109909.

[17] H. Huang, X. Tang, F. Chen, J. Liu, X. Sun, L. Ji, Radiation tolerance of nickel–graphene nanocomposite with disordered graphene, J. Nucl. Mater. 510 (2018) 1–9, https://doi.org/10.1016/j.jnucmat.2018.07.051.

[18] K. Yang, P. Tang, Q. Zhang, H. Ma, E. Liu, M. Li, X. Zhang, J. Li, Y. Liu, T. Fan, R. Namakian, Enhanced defect annihilation capability of the graphene/copper interface: an in situ study, Scripta Mater. 203 (2021) 114001, https://doi.org/10.1016/j.scriptamat.2021.114001.

[19] Z. Zou, L. Fu, X. Song, Y. Zhang, Z. Liu, Carbide-forming groups IVB-VIB metals: a new territory in the periodic table for CVD growth of graphene, Nano Lett. 14 (2014) 3832–3839, https://doi.org/10.1021/nl500994m.

[20] K. Chu, F. Wang, X. Wang, Y. Li, Z. Geng, D. Huang, H. Zhang, Interface design of graphene/copper composites by matrix alloying with titanium, Mater. Design 144 (2018) 290–303, https://doi.org/10.1016/j.matdes.2018.02.038.

[21] Y. Liu, S. Zhang, Y. Yao, L. Fan, J. Wang, Y. Wu, L. Jing, P. Han, C. Zhang, Enhancement of strength-ductility synergy of in situ synthesized graphene/Ni composite via Mo microalloying, Mater. Sci. Eng. A 919 (2025) 147496, https://doi.org/10.1016/j.msea.2024.147496.

[22] K.P. So, D. Chen, A. Kushima, M. Li, S. Kim, Y. Yang, Z. Wang, J.G. Park, Y.H. Lee, R.I. Gonzalez, M. Kiwi, E.M. Bringa, L. Shao, J. Li, Dispersion of carbon nanotubes in aluminum improves radiation resistance, Nano Energy 22 (2016) 319–327, https://doi.org/10.1016/j.nanoen.2016.01.019.

[23] X. Ge, Y. Jiang, X. Yu, G. Zhang, Y. Shi, B. Cai, Q. Peng, H. Huang, Preparation and characterization of graphene nanosheets-reinforced Ni-17Mo alloy composites for advanced nuclear reactor applications, Materials (Basel) 18 (2025) 1061, https://doi.org/10.3390/ma18051061.

[24] M.B. Eskandarkolaie, M. Rajabi, M. Amirnejad, M.T. Parizi, A. Pourghaz, Reduced graphene oxide (rGO) reinforced CoCrFeNiMn high entropy alloy: microstructure, mechanical properties, and corrosion behavior, Ceram. Int. 50 (2024) 29503–29517, https://doi.org/10.1016/j.ceramint.2024.05.246.

[25] H. Cao, Y. Liang, The microstructures and mechanical properties of graphene-reinforced titanium matrix composites, J. Alloy. Compd. 812 (2020) 152057, https://doi.org/10.1016/j.jallcom.2019.152057.

[26] Z. Zheng, Z. Zhang, L. Dong, G. Sun, J. Xu, M. Li, L. Li, Y. Zhang, Effects of carbon nanomaterials on interfacial structure and mechanical properties of high temperature Ti matrix composites, J. Alloy. Compd. 969 (2023) 172360, https://doi.org/10.1016/j.jallcom.2023.172360.

[27] B. Xiong, K. Liu, Q. Yan, W. Xiong, X. Wu, Microstructure and mechanical properties of graphene nanoplatelets reinforced Al matrix composites fabricated by spark plasma sintering, J. Alloy. Compd. 837 (2020) 155495, https://doi.org/10.1016/j.jallcom.2020.155495.

[28] Y. Gao, G. Zhang, H. Wang, J. Zou, Y. Han, Effect of the lateral area of graphene nanosheets on the strengthening mechanism in FGH96 superalloy composites, Carbon N Y 229 (2024) 119525, https://doi.org/10.1016/j.carbon.2024.119525.

[29] A.F. Rowcliffe, L.K. Mansur, D.T. Hoelzer, R.K. Nanstad, Perspectives on radiation effects in nickel-base alloys for applications in advanced reactors, J. Nucl. Mater. 392 (2009) 341–352, https://doi.org/10.1016/j.jnucmat.2009.03.023.

[30] M.A. Stopher, The effects of neutron radiation on nickel-based alloys, Mater. Sci. Tech. 33 (2017) 518–536, https://doi.org/10.1080/02670836.2016.1187334.

[31] A. Xu, M. Saleh, T. Wei, T. Palmer, H. Huang, D. Bhattacharyya, Investigating the effect of helium ion irradiation on deformation behaviour of Ni-Mo-Cr alloy via in-situ micro-tensile testing, J. Nucl. Mater. 567 (2022) 153812, https://doi.org/10.1016/j.jnucmat.2022.153812.

[32] S. Plimpton, Fast parallel algorithms for short-range molecular dynamics, J. Comput. Phys. 117 (1995) 1–19, https://doi.org/10.1006/jcph.1995.1039.

[33] A. Stukowski, Visualization and analysis of atomistic simulation data with OVITO–the Open Visualization Tool, Model. Simul. Mater. Sci. 18 (2009) 015012, https://doi.org/10.1088/0965-0393/18/1/015012.

[34] H. Huang, X. Tang, F. Chen, F. Gao, Q. Peng, L. Ji, X. Sun, Self-healing mechanism of irradiation defects in nickel-graphene nanocomposite: an energetic and kinetic perspective, J. Alloy. Compd. 765 (2018) 253–263, https://doi.org/10.1016/j.jallcom.2018.06.162.

[35] G. Bonny, N. Castin, D. Terentyev, Interatomic potential for studying ageing under irradiation in stainless steels: the FeNiCr model alloy, Model. Simul. Mater. Sci. 21 (2013) 085004, https://doi.org/10.1088/0965-0393/21/8/085004.

[36] S.J. Stuart, A.B. Tutein, J.A. Harrison, A reactive potential for hydrocarbons with intermolecular interactions, J. Chem. Phys. 112 (2000) 6472–6486, https://doi.org/10.1063/1.481208.

[37] K.O.E. Henriksson, C. Björkas, K. Nordlund, Atomistic simulations of stainless steels: a many-body potential for the Fe–Cr–C system, J. Phys. Condens. Mat. 25 (2013) 445401, https://doi.org/10.1088/0953-8984/25/44/445401.

[38] J.F. Ziegler, J. Biersack, U. Littmark, The Stopping and Range of Ions in Matter, vol. 1, Pergamon, New York, 1985. https://doi.org/10.1007/978-1-4615-8103-1_3.

[39] A. Ustrzycka, F.J. Dominguez-Gutierrez, W. Chromiński, Atomistic analysis of the mechanisms underlying irradiation-hardening in Fe–Ni–Cr alloys, Int. J. Plasticity 182 (2024) 104118, https://doi.org/10.1016/j.ijplas.2024.104118.

[40] M. Jin, P. Cao, M.P. Short, Mechanisms of grain boundary migration and growth in nanocrystalline metals under irradiation, Scripta Mater. 163 (2019) 66–70, https://doi.org/10.1016/j.scriptamat.2018.12.038.

[41] X. Bai, A.F. Voter, R.G. Hoagland, M. Nastasi, B.P. Uberuaga, Efficient annealing of radiation damage near grain boundaries via interstitial emission, Science 327 (2010) 1631–1634, https://doi.org/10.1126/science.1183723.

[42] P.M. Larsen, S. Schmidt, J. Schiøtz, Robust structural identification via polyhedral template matching, Model. Simul. Mater. Sci. 24 (2016) 055007, https://doi.org/10.1088/0965-0393/24/5/055007.

[43] J. Tian, Q. Feng, J. Zheng, X. Liu, W. Zhou, Radiation damage buildup and basal vacancy cluster formation in hcp zirconium: a molecular dynamics study, J. Nucl. Mater. 551 (2021) 152920, https://doi.org/10.1016/j.jnucmat.2021.152920.

[44] M. Jin, P. Cao, M.P. Short, Thermodynamic mixing energy and heterogeneous diffusion uncover the mechanisms of radiation damage reduction in single-phase Ni-Fe alloys, Acta Mater. 147 (2018) 16–23, https://doi.org/10.1016/j.actamat.2017.12.064.

[45] A.C. Ferrari, J. Robertson, Interpretation of Raman spectra of disordered and amorphous carbon, Phys. Rev. B 61 (2000) 14095, https://doi.org/10.1103/PhysRevB.61.14095.

[46] F.R. Eder, J. Kotakoski, U. Kaiser, J.C. Meyer, A journey from order to disorder—Atom by atom transformation from graphene to a 2D carbon glass, Sci. Rep. 4 (2014) 4060, https://doi.org/10.1038/srep04060.

[47] C. Pan, J.A. Hinks, Q.M. Ramasse, G. Greaves, U. Bangert, S.E. Donnelly, S. J. Haigh, In-situ observation and atomic resolution imaging of the ion irradiation induced amorphisation of graphene, Sci. Rep. 4 (2014) 6334, https://doi.org/10.1038/srep06334.

[48] B. Song, G.F. Schneider, Q. Xu, G. Pandraud, C. Dekker, H. Zandbergen, Atomic-scale electron-beam sculpting of near-defect-free graphene nanostructures, Nano Lett. 11 (2011) 2247–2250, https://doi.org/10.1021/nl200369r.

[49] S. Karoui, H. Amara, C. Bichara, F. Ducastelle, Nickel-assisted healing of defective graphene, ACS Nano 4 (2010) 6114–6120, https://doi.org/10.1021/nn101822s.
[50] P. Jacobson, B. Stöger, A. Garhofer, G.S. Parkinson, M. Schmid, R. Caudillo, F. Mittendorfer, J. Redinger, U. Diebold, Disorder and defect healing in graphene on Ni (111), J. Phys. Chem. Lett. 3 (2012) 136–139, https://doi.org/10.1021/jz2015007.
[51] A. Suhane, D. Scheiber, M. Popov, V.I. Razumovskiy, L. Romaner, M. Militzer, Solute drag assessment of grain boundary migration in Au, Acta Mater 224 (2022) 117473, https://doi.org/10.1016/j.actamat.2021.117473.
[52] J. Li, J. Wang, G. Yang, Phase field modeling of grain boundary migration with solute drag, Acta Mater. 57 (2009) 2108–2120, https://doi.org/10.1016/j.actamat.2009.01.003.
[53] W. Sun, H.S. Zurob, C.R. Hutchinson, Coupled solute drag and transformation stasis during ferrite formation in Fe-C-Mn-Mo, Acta Mater. 139 (2017) 62–74, https://doi.org/10.1016/j.actamat.2017.08.010.
[54] Z. Dai, H. Chen, J. Sun, S. van der Zwaag, J. Sun, Carbon solute drag effect on the growth of carbon supersaturated bainitic ferrite: modeling and experimental validations, Acta Mater. 268 (2024) 119791, https://doi.org/10.1016/j.actamat.2024.119791.